ORIGINAL RESEARCH

Remote sensing data fusion as a tool for biomass prediction in extensive grasslands invaded by *L. polyphyllus*

Damian Schulze-Brüninghoff (iD), Michael Wachendorf, Prof. Dr. (iD) & Thomas Astor, Dr. (iD)

Grassland Science and Renewable Plant Resources, Faculty of Organic Agricultural Science, Universität Kassel, Steinstrasse 19, Witzenhausen D-37213, Germany Open access funding enabled and organized by Projekt DEAL.

Abstract

Remote sensing data fusion is a powerful tool to gain information of quantitative and qualitative vegetation properties on field level. The aim of this study was to develop prediction models from sensor data fusion for fresh and dry matter yield (FMY/DMY) in extensively managed grasslands with variable degree of invasion by *Lupinus polyphyllus*. Therefore, a terrestrial 3d laser scanner (TLS) and a drone-based hyperspectral camera was used to collect high resolution 3d point clouds and hyperspectral aerial orthomosaics of four extremely heterogenous grasslands. From 3d point clouds multiple features (vegetation height, sum of voxel, point density and surface structure) were extracted and combined with hyperspectral data to develop an optimized biomass model from random forest regression algorithm to predict FMY and DMY ($n_{train} = 130$, $n_{test} = 33$). Models from hyperspectral data solitarily had the lowest prediction performance (FMY: $R^2 = 0.61$, $nRMSE_r = 17.14$; DMY: $R^2 = 0.59$, $nRMSE_r = 19.37$). Higher performance was gained by models derived from 3d laser data (FMY: $R^2 = 0.76$, $nRMSE_r = 13.3$; DMY: $R^2 = 0.74$, $nRMSE_r = 15.1$). A fusion of both sensor systems increased the FMY prediction performance up to $R^2 = 0.8$; $nRMSE_r = 12.02$ and the DMY prediction performance to $R^2 = 0.81$ and $nRMSE_r = 12.06$. The fusion of complementary sensor systems can increase the power to predict biomass yields of heterogenous and extensively managed grasslands. It is a novel alternative to labour-intensive, traditional biomass prediction methods and to remote sensing methods using only single sensor data.

Introduction

Grasslands are one of the main land cover types in Europe and cover more than a third of the agricultural used area (Smit et al., 2008). Permanent grasslands have a high contribution in providing ecosystem services (de Bello et al., 2010). But heterogenous, extensive grasslands are at risk of the spread of invasive plant species which pose a significant impact from ecosystem, over community, down to species level (Vilà et al., 2011). One species affecting heterogenous and highly divers grasslands is *Lupinus polyphyllus L.* (hereafter referred to as lupine), a perennial, nitrogen-fixing plant, that originated in North America (Hackbart, 1961) and was first described in Europe in 1827 by John Lindley. It was brought to Europe as an ornamental plant, but in

the 1880s it was used as a cover crop in forestry. Today, lupine invasive appearance is observed in many European countries. The invasion of nitrogen-fixing plants can lead to declines in biodiversity, soil acidification and alterations to carbon and nutrient cycling trough leaching and N_2O emissions (Valtonen et al., 2006; Hiltbrunner et al., 2014). The spread of lupine substantially affects the vertical structure of invaded grasslands and causes a decline in species richness (Otte and Maul, 2005).

Monitoring and managing invaded grasslands have become more crucial and remote sensing measurement techniques provide promising approaches and are already in the focus of agricultural research (Weiss et al., 2020). As technical equipment is improved and computational power increases, the ability to process larger remote

sensing data is becoming much more feasible. At the same time, new processing methods like machine learning evolve, unlocking the potential to deal with often highly autocorrelated features from remote sensing data (Gewali et al., 2018). A further step towards an optimized prediction of heterogenous grassland biomass is the utilization of multiple complementary sensor systems (Wachendorf et al., 2017).

Non-destructive measurements of above-ground biomass are fundamental to understand anthropogenic and environmental influences on ecosystems. While forestry (White et al., 2016), arable crops (Weiss et al., 2020) and high input grassland systems (Ali et al., 2017) are mainly in the focus of remote sensing research methods, above-ground biomass from extensively used, highly heterogenous grasslands is still challenging to measure accurately. Using different sensor systems which for example combine three-dimensional (3d) and spectral information could enhance the potential of biomass quantification in grasslands (Moeckel et al., 2017). Spectral information predominantly informs on leaf properties, since the absorption processes by individual leaves can indicate their constituents (e.g. starch, carbohydrates, water). Spectral reflectance also informs on scattering (predominantly in the near infrared region) and hereby informs on the amount of foliage in the canopy. However, LiDAR information is superior in resembling the canopy structure and the total amount of plant tissue, but it lacks information of leaf constituents. Hence, combining both sensor types has the potential to improve prediction of biomass. This study conducted measurements from drone-based hyperspectral imagery and from a terrestrial 3d laser scanner (TLS) to quantify fresh matter yield (FMY) and dry matter yield (DMY) for four extensive grassland sites, partly invaded by lupine. The specific aims were:

(1) To develop biomass prediction models for FMY and DMY in highly heterogenous, extensive grasslands, utilizing random forest regression machine learning with input of hyperspectral and/or 3d laser data in comparison.
(2) To Identify and evaluate the effect of the most important features for the FMY and DMY prediction models.
(3) To assess the effect of lupine presence on the FMY and DMY model accuracy.

Materials and Methods

Study area

The UNESCO biosphere reserve Rhön is a volcanic lower mountain range on the border of Hesse, Bavaria and Thuringia with an annual average precipitation of 1084 mm and a mean temperature of 4.8°C (Deutscher Wetterdienst, 2018). The study area at 750–840 m asl is characterized by a shortened vegetation period and a late spring. By the end of the 14th century the landscape transformed from beech forest to grasslands which were characterized by an extensive grazing and mowing regime (Kindinger, 1942). Today, the study area is characterized by versatile flora (e. g. *Trollius europaeus, Arnica montana*) and provides a habitat for endangered species like *Tetrao tetrix*. However, in the past decades, lupine spread throughout the sites and is now partly dominating large areas (Volz, 2003). Sensor and reference data were collected at four sites (Fig. 1). Two sites were located in the state Hesse (50° 28' 44.0"N, 9° 58' 17.1"E and 50° 28' 58.4"N, 9° 59' 09.9"E), whereof one site was dominated by *Nardus stricta* (matgrass)) and one by *Trisetum flavescens* (golden oatgrass)). Two sites, located in Bavaria (*Nardus stricta*: 50° 28' 45.0"N, 10° 02' 34.6"E and *Trisetum flavescens*: 50° 29' 17.1"N, 10° 03' 40.9"E), were highly invaded by lupine.

Data acquisition

Sampling dates were at 15 June, 27 June and 11 July 2018. At each site five plots were sampled at each sampling date. The plot size was 8 × 8 metres. For each sampling date first drone-based hyperspectral data and 3d laser scanner data were collected. Afterwards ground based (destructive) reference data were sampled. Hyperspectral data were collected using a Firefly S185 SE (Cubert GmbH, Germany) snapshot camera mounted on a UAV RTK X8 (Copter Squad UAS UG, Germany). The spectral range is between 450 and 998 nm and covers 138 bands with 4 nm sampling interval. Due to low signal-to-noise ratios in the highest and lowest spectral bands, the spectral bands were reduced to a spectral range of 482 to 950 nm for further analysis. The spectral images have a size of 50 × 50 pixels and a radiometric resolution of 12 bit. An additional panchromatic band with an image size of 1000 x 990 pixels is recorded as well. Flight altitude was 20 m aboveground with a spatial resolution of ~20 cm for the spectral images and ~1 cm for the panchromatic band. Flight altitude was chosen as a compromise of high spatial resolution and avoidance of wind influence on the vegetation by the drone. An automated drone mission plan was configured with 3 ms^{-1} flight speed and an image forward overlap of 80% and side overlap of 60 %.

Before the flight, six ground control targets were distributed inside the study site and GPS coordinates were recorded using a Leica RTK GNSS (Leica Geosystems GmbH, Germany) with a 3d accuracy of ~1.5 cm. A radiometric calibration of the hyperspectral camera was conducted with a white calibration panel (95% reflectance) and a dark calibration using the lens cap.
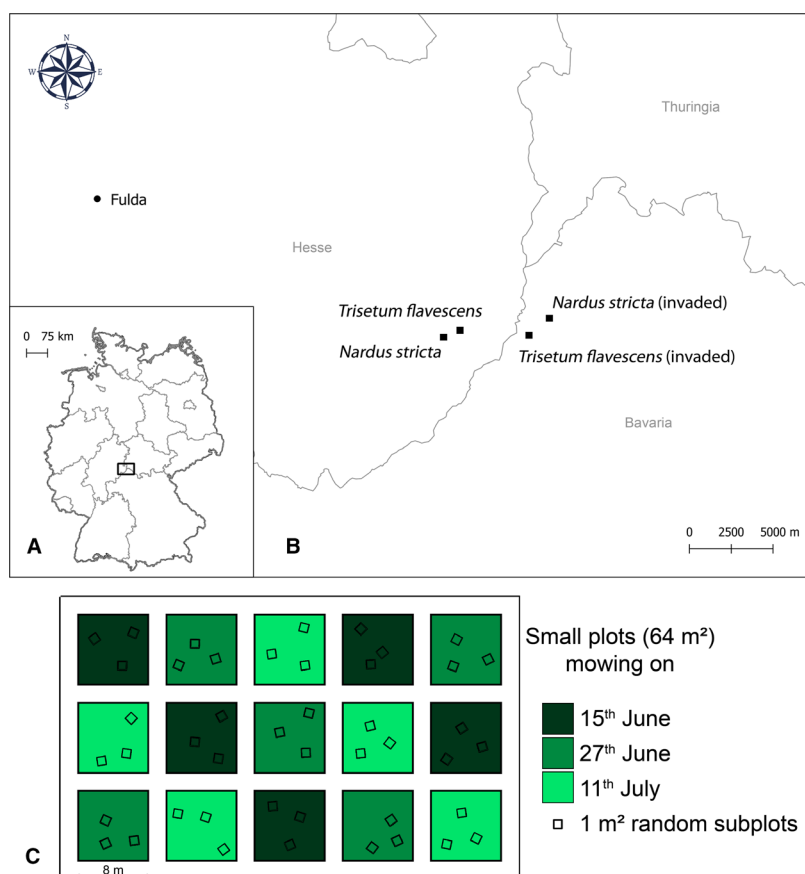
Figure 1. (A) Location of the Study area in the biosphere reserve 'Rhön'. (B) *Nardus stricta* and *Trisetum flavescens* grassland in Hesse and invaded by *L. polyphyllus* in Bavaria. (C) Experimental plot design for each study grassland. Subplot sampling for reference data was done once according to the date of mowing.

The 3d laser scanning was performed using a Leica Scan Station P30 (Leica Geosystems GmbH, Germany) with a spatial resolution of 1.6 mm at 10 m distance. Each plot was scanned from two (opposite) directions at a distance of ~1.5 m and a height of ~1.75 m based on the methods described in detail in Schulze-Brüninghoff et al. (2019). Three tripod targets were placed nearby the scanner for georeferencing and merging of the point clouds. Each site was scanned using a 3d laser scanner in spring with marginal vegetation to provide a digital elevation model (DEM).

For destructive biomass sampling, in each plot, the GPS coordinates of the corners of three randomly selected 1 m^2 subplots were measured. Subplot biomass was cut at 5 cm height, and lupine was separated. Fresh biomass and lupine biomass were separately measured and dried at 105°C for 48 h for measuring dry biomass.

Due to wrong z coordinate values in the DEM point cloud, the samples from lupine free *Trisetum flavescens* grassland at first harvesting date ($n = 15$) had to be excluded from datasets. Additionally, two samples from the same site at second harvesting date had to be excluded, as they showed very unusual spectral reflectance pattern due to overexposure in image capturing.

Pre-processing hyperspectral data

To gain hyperspectral orthomosaics, raw Cubert data were exported as multi tiff files by CubeExport DOS command (Cubert GmbH, Germany). Those 50 × 50 pixel hyperspectral images were disaggregated 20 times by nearest neighbour resampling and stacked with a panchromatic 1000x990 pixel image with the R-package *raster* (Hijmans, 2019). Afterwards, image stacks were imported to Agisoft PhotoScan Professional software version 1.4.1 (Agisoft LLC, Russia) for image stitching. We generated orthomosaics from surface reflectance images. This means, orthomosaics have actual ground reference. To avoid mixing pixels when mosaicking images, we selected just the *mosaic* option in agisoft instead of *average*. Orthomosaics

were processed, using the ground control points for geo-referencing and increasing the stitching accuracy. Afterwards, the panchromatic band was removed. Reference subplots were cut out from orthomosaics and spectral reflectance for each band was averaged for each subplot. The spectral reflectance curve of each subplot was normalized by vector normalization (Eq. 1), where x_i is the spectral vector for $i = 1, 2,..., n$ (Sun et al., 2015).

$$rx_i = \frac{x_i}{\sqrt{\sum \| x_i \|^2}} \tag{1}$$

Pre-processing 3d laser data

Two point clouds of each plot were merged in Cyclone 9.1 software (Leica Geosystems GmbH, Germany). The tripod targets were used for merging and georeferencing the point clouds. Unrealistic, solitaire points were deleted manually. Afterwards, each 1 m^2 subplot was cut out. Multiple features were extracted for each 1 m^2, (a) Canopy Surface Height (CSH), (b) Sum of Voxel and (c) Canopy Surface Elevation, Slope and Curvature as well as point density were calculated (Fig. 2).

Canopy surface height

For each point of the cloud the point height was calculated by subtracting the corresponding z values of the digital elevation model (DEM) from the z coordinate value of the point cloud. The DEM is a raster dataset with 0.05-m resolution, derived from a point cloud, scanned with the same TLS system in spring 2018 with marginal vegetation. For each raster cell, the minimum height value of the DEM point cloud was used to gain the raster cell height. Calculations were done in R statistical software (R Core Team, 2019) with the *raster* R-package (Hijmans, 2019). The point cloud was subdivided on vertical level (height) in different percentiles ranging from 1 to 99 %. For each percentile (e. g. the upper 45 % of (Fig. 2A)) the mean CSH value was calculated.

Sum of voxel

A group of voxels is a digital representation of a volumetric object. For biomass prediction, each subplot's point cloud is subdivided into voxels with an arbitrarily defined
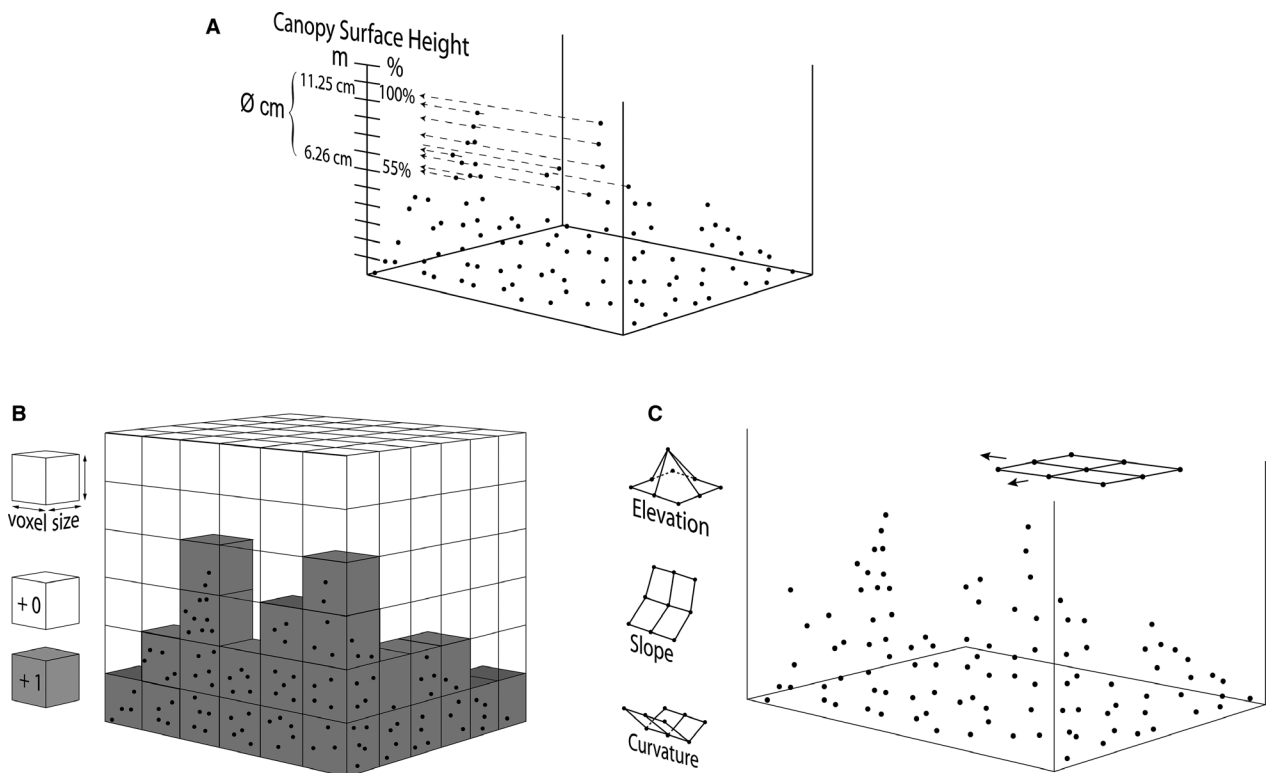
Figure 2. Methods for 3d-laser feature extraction. (A) CSH extraction. The figure displays the example of a mean CSH calculation for the upper 55% of the point cloud. (B) Sum of Voxel. Each Voxel that contains at least one point inside is counted with + 1 to the Sum of Voxel. (C) Canopy Surface Elevation, Slope and Curvature. With 9 by 9 matrix which is applied to the point cloud to check for its surface structure by calculating elevation, slope and curvature values for the centre of the matrix.

size. To calculate the Sum of Voxel, function *vox* from R-package *VoxR* (Lecigne et al., 2014) was utilized. Each voxel applied to the subplot was checked for, whether a point of the point cloud is located inside the voxel or whether the voxel is empty. Each voxel, representing a volumetric space in the subplot, containing at least one point of the point cloud, is added to the Voxel-Sum. Sum of Voxel was calculated for Voxel edge lengths varying from 5 mm to 30 cm, considering best prediction performance for FMY and DMY in this range as shown by Schulze-Brüninghoff et al. (2019).

Point density

The point cloud is subdivided into 0.02 cm grid cells by function *raster* from *raster* package (Hijmans, 2019). Point density is calculated for quantiles of 0.25, 0.5 and 0.75 by function rasterize from the same package, applied in each grid cell and averaged for each subplot.

Canopy surface structure

Surface structure was calculated in terms of slope, elevation and curvature from R-package *raster* (Hijmans, 2019) as a collection of four different mathematical approaches described by Florinsky (1998). One approach (Evans, 1980) uses a polynomial (Eq. 2) approximated by the least square method to a 3 by 3 altitude submatrix (Fig. 3).

$$z = \frac{rx^2}{2} + \frac{ty^2}{2} + sxy + px + py + u \tag{2}$$

For the centre of the matrix the formulae for coefficients r, t, s, p, q (Eq. 3–7) of the polynomial are:

$$r = \frac{z1 + z3 + z4 + z6 + z7 + z8 - 2(z2 + z5 + z8)}{3w^3} \tag{3}$$

$$t = \frac{z1 + z2 + z3 + z7 + z8 + z9 - 2(z4 + z5 + z6)}{3w^2} \tag{4}$$

$$s = \frac{z3 + z7 - z1 - z9}{4w^2} \tag{5}$$

$$p = \frac{z3 + z6 + z9 - z1 - z4 - z7}{6w} \tag{6}$$

$$q = \frac{z1 + z2 + z3 - z7 - z8 - z9}{6w} \tag{7}$$

From these values, slope gradient (G), aspect (A), horizontal (k_h) and vertical (k_v) surface curvature can be calculated (Eqs. 8–11).

$$G = \tan^{-1}\left(\sqrt{p^2 + q^2}\right) \tag{8}$$
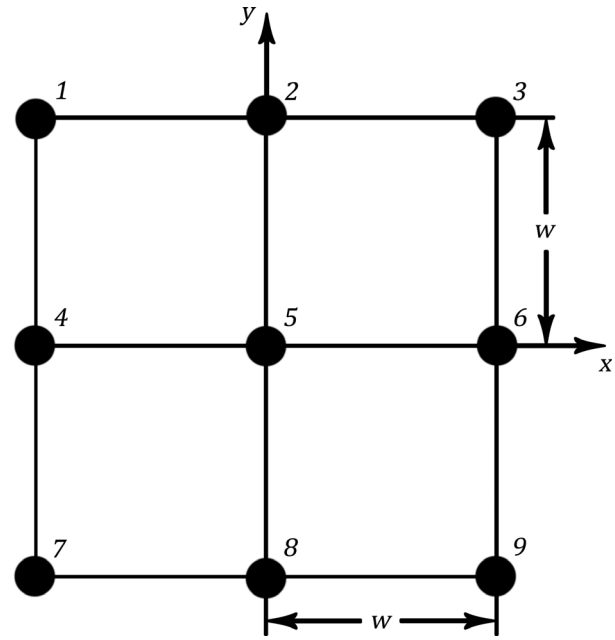
$$A = \tan^{-1}\left(\frac{q}{p}\right) \tag{9}$$

Figure 3. A 3 by 3 submatrix with grid mesh w and nodes z1, ... z9.

$$k_h = \frac{q^2r - 2pqs + p^2t}{(p^2 + q^2)\sqrt{1 + p^2 + q^2}} \tag{10}$$

$$k_v = \frac{p^2r + 2pqs + q^2t}{(p^2 + q^2)\sqrt{(1 + p^2 + q^2)^3}} \tag{11}$$

For each G, k_h and k_v the range and mean value was calculated.

Independent from this approach, an elevation-mean and elevation-variance value was calculated. Therefore, the point cloud was subdivided into 0.02 m grid cells. For each cell, the maximum CSH value was extracted. From these values, the mean and variance were calculated.

Feature selection

A three-step feature selection ('thresholding', 'interpretation', 'prediction') was run by function *VSURF* from R-package *VSURF* (Genuer et al., 2019) to simplify the model's data input for a random forest regression model. All arguments were kept at default value.

The first step ('thresholding step') eliminated irrelevant features by ranking the feature importance and computing a threshold for the standard deviations of feature importance (from 50 random forest runs), since meaningful features have a larger standard deviation compared to features of small importance. This threshold was the minimum predicted value of a pruned CART tree fitted to the curve of the standard deviations of feature
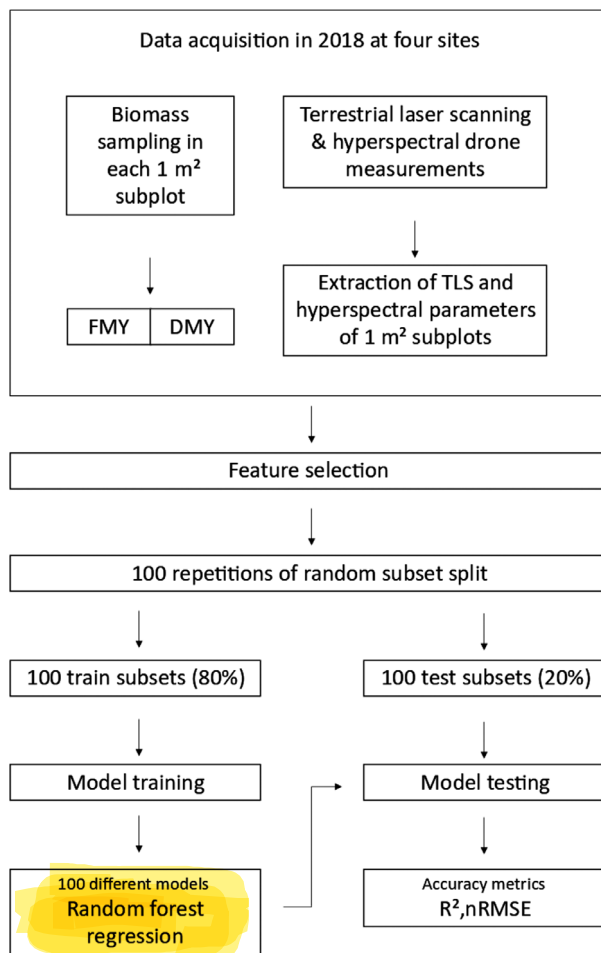
Figure 4. Workflow of model development. FMY, fresh matter yield; DMY, dry matter yield; TLS, terrestrial laser scanner; RMSE, root mean square error; nRMSEr, RMSE normalised by the range of the observation.

importance. Then, only features with a mean importance exceeding this threshold were retained.

The subset from second step ('interpretation step') still includes features with redundancy for interpretation purposes. Therefore, out-of-bag error rates (Breiman, 2001) of random forests (25 runs) were computed, starting with only the most important feature. The final feature set was selected from the model with an OOB error less than the minimal OOB error augmented by its standard deviation (to deal with instability).

The subset from third step ('prediction step') was for prediction objectives and used for our final models. Here, the ranked features from 'interpretation step' were invoked and tested. A feature was only added, if the OOB error decrease was significantly greater than the average variation obtained by adding noisy features.

Model development

Model development was done in R statistical software (R Core Team, 2019). Random forest regression (Breiman, 2001), a machine learning approach, was chosen to predict grassland FMY and DMY from highly correlated hyperspectral features, as well as 3d laser-based features. Training and test subsets for random forest regression models (R-package *caret* (Kuhn, 2008)) were split randomly 100 times to explain the variability in model performance within the data subset (Fig. 4). Sample splitting was stratified by the four different grassland sites. Metrics to evaluate model performance were the median R^2 and median nRMSE$_r$ which is the RMSE (Eq. 12) normalized by range of the biomass values of the observation (Eq. 13).

$$RMSE = \sqrt{\frac{1}{n}\sum_{j=1}^{n}\left(y_j - y_j\right)^2} \qquad (12)$$

$$nRMSEr = \frac{RMSE}{y_{max} - y_{min}} \times 100 \qquad (13)$$

Normalized deviation of predicted and measured FMY and DMY were calculated (Eq. 14) and the effect of sampling sites and contribution of lupine on the model prediction was examined.

$$Normalised\ deviation = \frac{Predicted\ biomass - Observed\ biomass}{Predicted\ biomass + Observed\ biomass} \qquad (14)$$

The most important features, for all 100 prediction models, were identified by *varImp* function from R-package *caret* (Kuhn, 2008). The importance of a feature is received by looking at how much the prediction error increases (%IncMSE) when (out-of-bag – cf. Breiman, (1996)) data for that feature are permuted while all others are left unchanged. The calculations are carried out tree by tree. Further, %IncMSE is then divided by its standard deviation and has been scaled to 0–100%.

Additionally, ALE (Accumulated Local Effects) plots were created for the four most important feature types (a type is the collection of e. g. all CSH features) of each FMY and DMY prediction model from laser and hyperspectral sensor alone and in combination. As features from the same feature type have similar a pattern in ALE plots, only one per type was illustrated. Calculation was done with R-package *ALEPlot* (Apley, 2018). ALE plots are applicable on datasets which have strongly correlated predictors, to visualize the effects of the predictors in machine learning models. ALE plots not only consider correlation of multiple predictors, they also avoid mixing the effect of a feature with the effect of all correlated features, as correlated features do not have
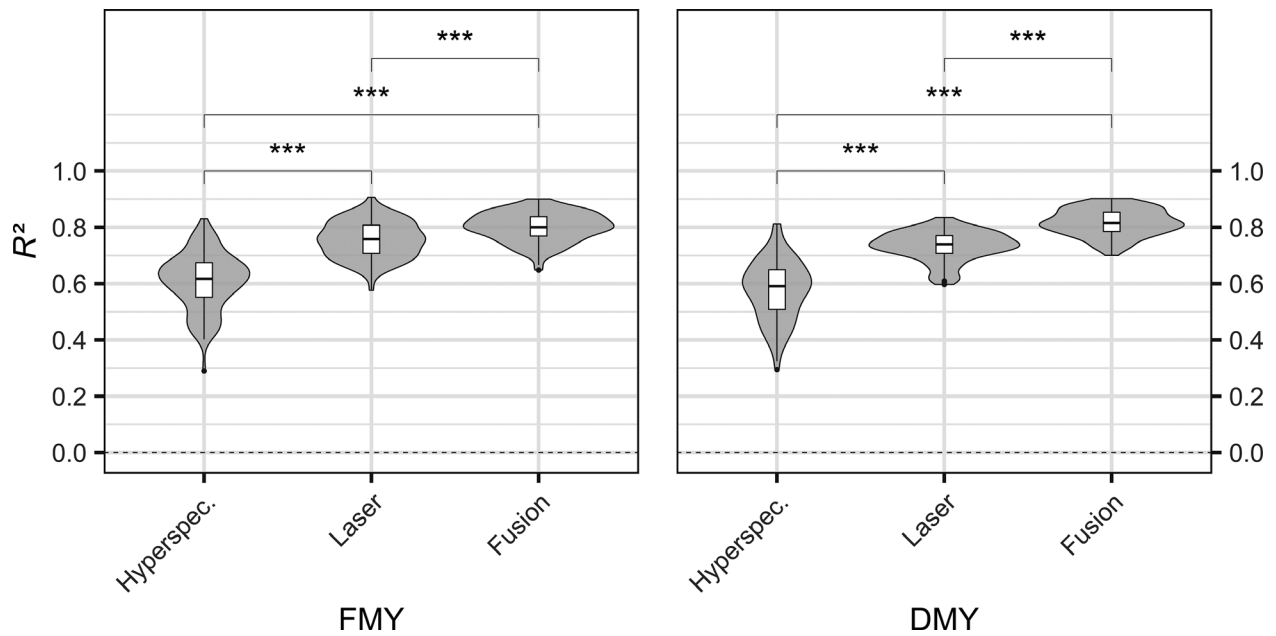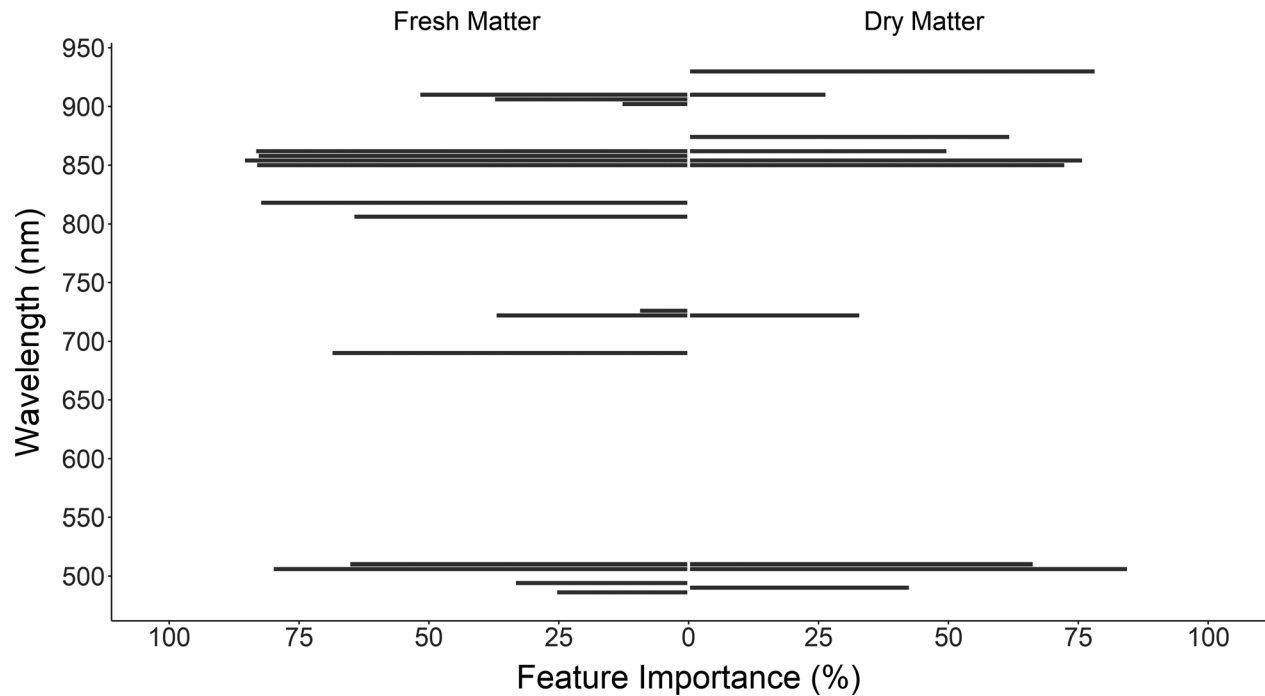
Figure 5. Comparison of R^2 of FMY and DMY prediction models for single sensor data and sensor data fusion. Boxplots represent hundred different random forest regression model runs each. ***$P < 0.001$.
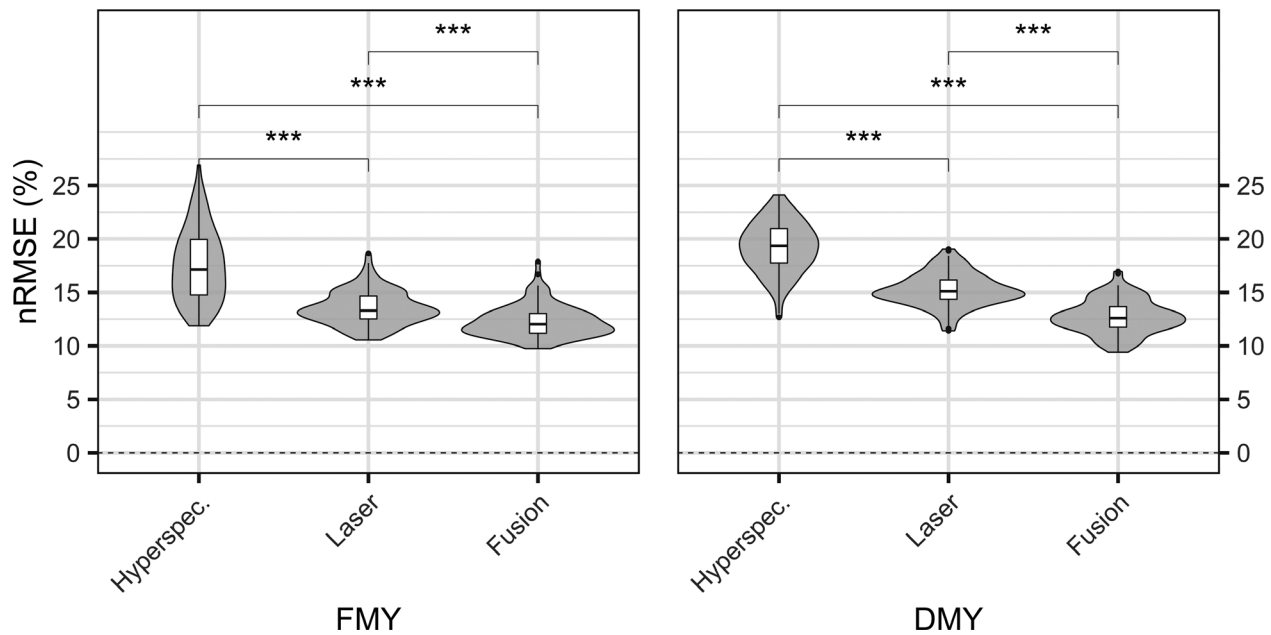
Figure 6. Comparison of nRMSEr of FMY and DMY prediction models for single sensor data and sensor data fusion. Boxplots represent hundred different random forest regression model runs each. ***$P < 0.001$.

inevitably an effect on the prediction value (Apley and Zhu, 2019). The ALE method divides each feature into intervals. For the data instances in a single interval, the difference in prediction is calculated when the feature is replaced by the upper and lower limit of the interval.

Later, the difference of each interval is accumulated, centred and visualized in a plot. The ALE value can be interpreted as the main effect of the feature at a certain value compared to the average prediction of the data (Apley and Zhu, 2019).

© 2020 The Authors. *Remote Sensing in Ecology and Conservation* published by John Wiley & Sons Ltd on behalf of Zoological Society of London.

Figure 7. Contribution of hyperspectral bands to predict FMY and DMY for random forest regression model built with hyperspectral data only (importance as median from 100 different random forest regression model runs).

Results

FMY varied between 0.05 kg m^{-2} and 3.07 kg m^{-2}, DMY between 0.02 kg m^{-2} and 0.54 kg m^{-2} (Table S1). Yields from *Nardus stricta* grassland were lower than all other three sites (Table S2).

Models from hyperspectral data solitarily had the lowest prediction performance (FMY: $R^2 = 0.61$, nRMSE$_r$ = 17.14; DMY: $R^2 = 0.59$, nRMSE$_r$ = 19.37). Higher performance was gained by models derived from 3d laser data (FMY: $R^2 = 0.76$, nRMSE$_r$ = 13.3; DMY: $R^2 = 0.74$, nRMSE$_r$ = 15.1). A fusion of both sensor systems increased the FMY prediction performance up to $R^2 = 0.8$; nRMSE$_r$ = 12.02 and the DMY prediction performance to $R^2 = 0.81$ and nRMSE$_r$ = 12.06 (Figs. 5 and 6).

From hyperspectral sensor data, the feature importance metric as described in Section 2.5, which is scaled from 0 to 100%, was investigated.

Most important wavelengths contributing to the prediction of FMY were in the infrared range between 806 nm and 862 nm as well as in the visible (green) spectrum at 506–510 nm. For DMY, it ranged from 850 nm to 874 nm and from 506 to 510 nm. Additionally, the wavelength of 930 nm had a high importance (Fig. 7). For random forest regression models from laser data, high

contribution to prediction performance was based on multiple laser features (point density-, voxel-, surface structure- and height values). Random forest regression models from fusion data comprised important features by both, laser and hyperspectral sensor data. Spectral bands from 846 to 858 nm and CSH features had the highest importance in FMY prediction models, whereas a larger range of spectral bands between 674 nm and 950 nm as well as mean elevation and CSH features were most important in DMY prediction models (Fig. 8).

Normalized deviation of predicted and measured biomass was used to investigate if the abundance of lupine on field and subplot level affects FMY and DMY prediction by the RF models. *Nardus stricta* grassland in fresh and dry condition showed some overprediction, whereas, *Trisetum flavescens* showed a slight underprediction for DMY. Lupine invaded sites had normalized deviations comparable to *Trisetum flavescens*, both for FMY and DMY. *Nardus stricta* grassland had a higher range of deviation (Fig. 9).

Normalized deviation of predicted and measured FMY and DMY showed some overprediction of FMY and DMY at low lupine contributions and an underprediction at high lupine contributions. Between 20% and 40% of lupine contribution, the prediction model showed the lowest deviation (Figs. 10 and 11).
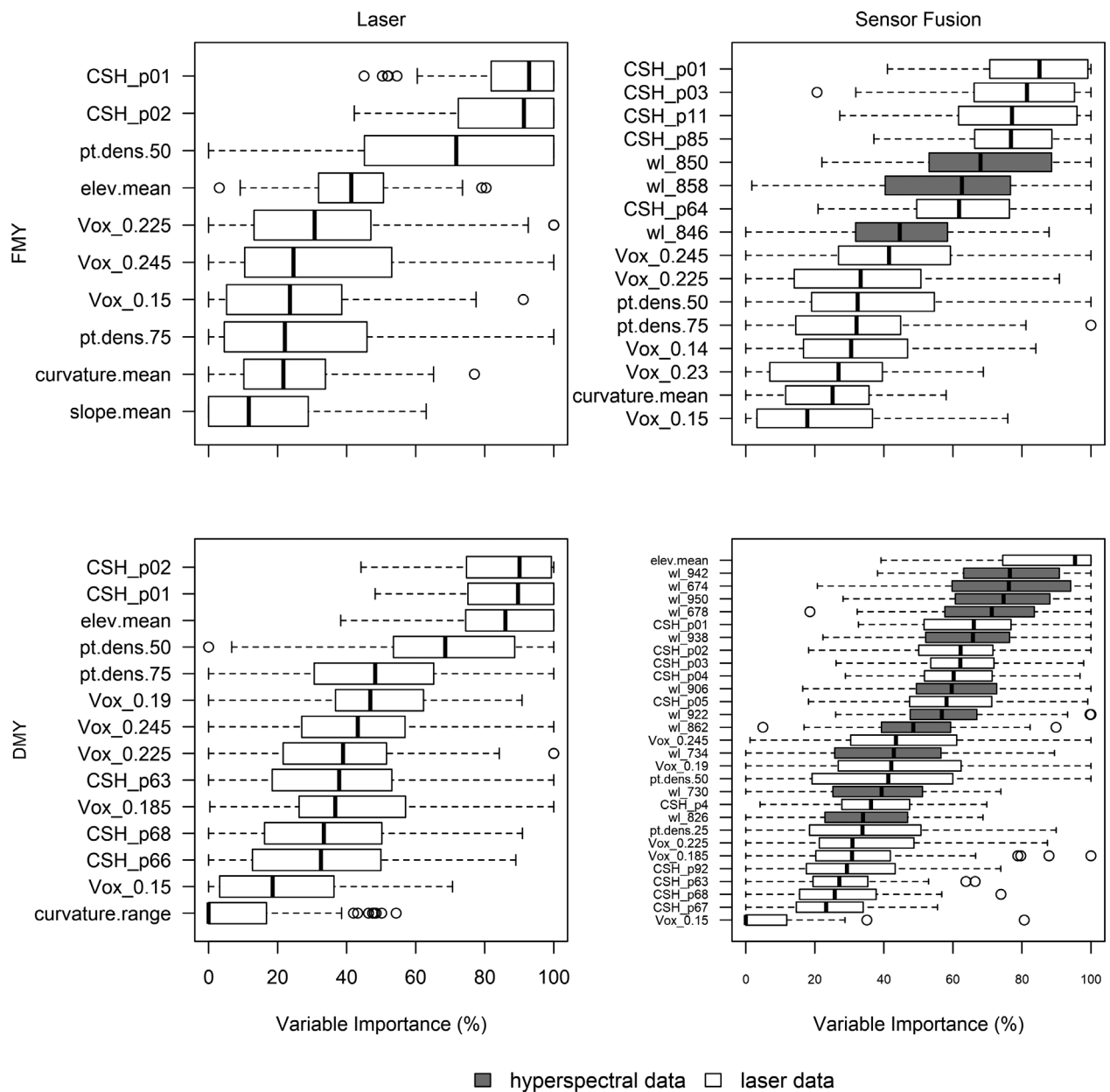
Figure 8. Features for each hundred FMY (top) and DMY (C, D) prediction models (bottom) from laser features only (left) and from sensor fusion data (right). Dark boxplots in sensor fusion model are features derived from hyperspectral data, white boxplots from laser data.

Discussion

The development of biomass prediction models for FMY and DMY in highly heterogenous, extensive grasslands has been successful (Fig. 13). Utilizing random forest regression with fusion of hyperspectral and 3d laser data achieved higher prediction accuracies compared to single sensor data. Hyperspectral data alone had the lowest prediction performance compared to laser data models and sensor fusion data models. This result is in line with other sensor fusion studies (Swatantran *et al.*, 2011; Wang et al., 2017; Lussem et al., 2019; Karunaratne et al., 2020). However, the sensor fusion model derived from this study could explain FMY and DMY in extremely heterogenous grasslands with the same accuracy as studies for homogenous vegetation structures (Swatantran et al., 2011; Yue et al., 2017). Swatantran et al. (2011) for example estimated winter wheat above-ground biomass using hyperspectral and crop height information and gained prediction accuracies of $R^2 = 0.74$, RMSE = 1.20 t ha^{-1}

Figure 9. Normalised deviation between predicted and measured FMY (left) and DMY (right) for all four grassland sites. NS, *Nardus stricta* grassland; NSL, *Nardus stricta* grassland invaded by lupine; TF, *Trisetum flavescens* grassland; TFL, *Trisetum flavescens* grassland invaded by lupine. Diamond points represent mean values.
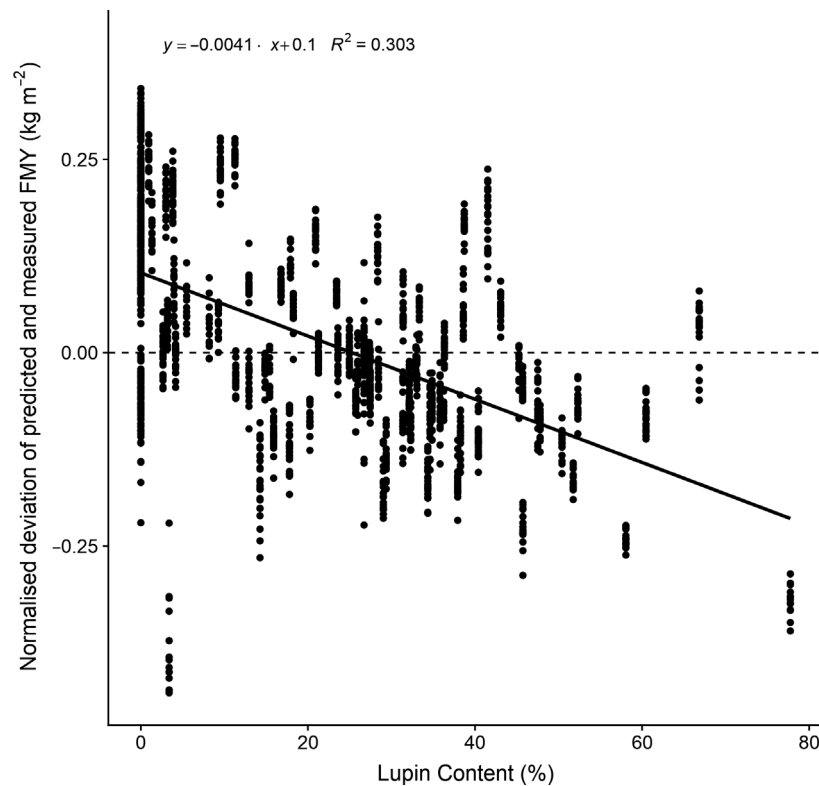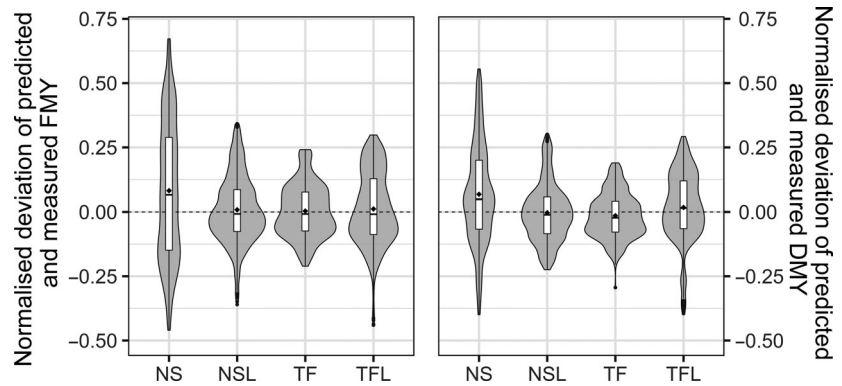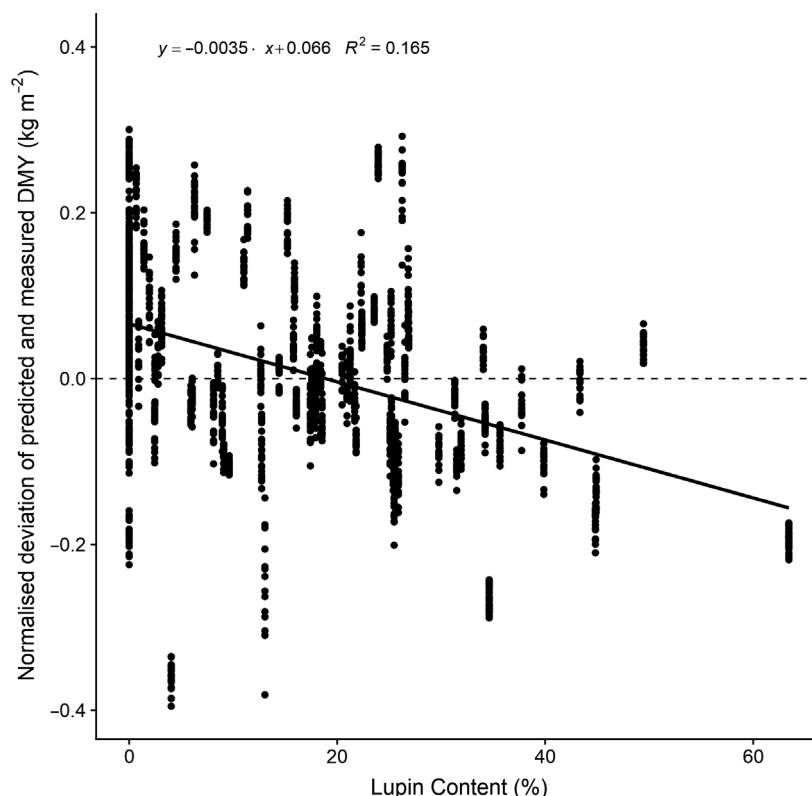

Figure 10. Normalised deviation between predicted and measured FMY for different contribution of lupine at each reference plot from lupine invaded grassland sites with hundred different model runs.

and MAE = 0.96 t ha^{-1}, which is comparable to our model performance and indicates the generalizability of machine learning methods using sensor fusion data to predict FMY and DMY. However, biomass of extensively managed grasslands can be challenging to predict when high contributions of dead plant material is present (Moeckel et al., 2017).

Considering feature importance in the FMY and DMY prediction models, the most important features from laser

data were point density, sum of voxel, CSH, elevation, curvature and slope features, which shows that 3d point cloud information is ideally used with a broad selection of feature types. Most important spectral wavebands for hyperspectral sensor models as well as for sensor fusion models were in the infrared region as well as in the visible green, and red range. These spectral regions are known for their sensitivity to physiological attributes and, thereby, for vegetation biomass yields. Therefore, visible

Figure 11. Random forest regression model: Normalised deviation between predicted and measured DMY for different contribution of lupine at each reference plot from lupine invaded grassland sites with hundred different model runs.
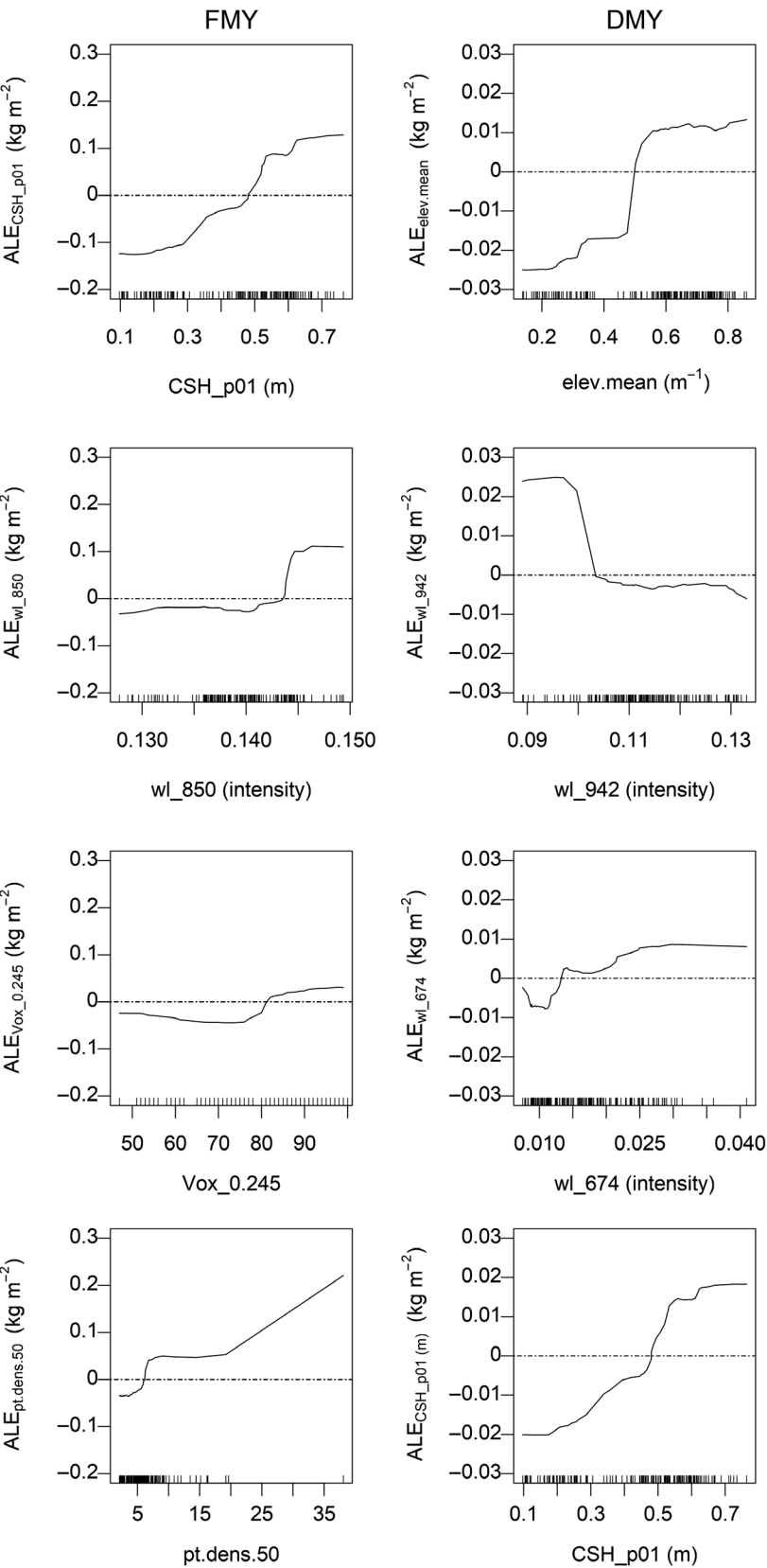
and near infrared spectra are commonly used in indices to predict biomass yields (Rouse et al., 1974; Silleos et al., 2006; Xue and Su, 2017; Kong et al., 2019).
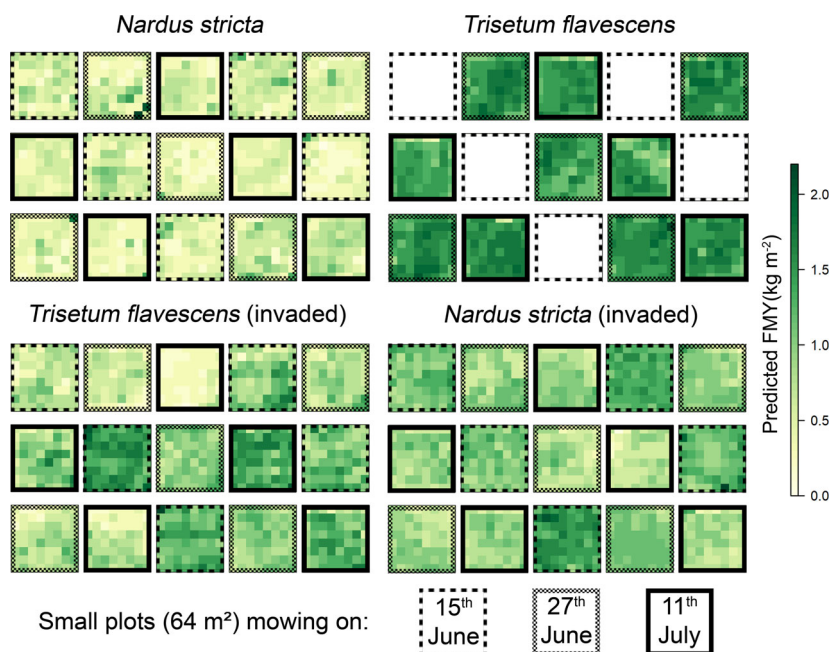
The fusion of both sensor systems increased the model prediction performance and for both, FMY and DMY prediction, the feature selection process included spectral features to the models. FMY prediction models comprised wavelengths around 846–858 nm, while DMY prediction models had wavelengths around 938–950 nm. The band region at 970 nm is a minor water absorption band (Clevers et al., 2008). As canopy water content (in kg m^{-2}) is the difference between FMY and DMY, and differences in canopy water content are visible in the spectral signature at 970 nm, accuracy of DMY prediction may be increased by considering the influence of water absorption. The near infrared and the red edge region have also been identified as important features for DMY prediction by Karunaratne et al. (2020) in the form of vegetation

indices. Especially for low flying altitude (25 m), they had a high number of spectral vegetation indices under their most important features.

To investigate the effect of the most important feature types on the FMY and DMY prediction models, ALE plots were used. For the effect of the hyperspectral band at 850 nm on FMY prediction it showed lower prediction yields for lower spectral intensities and higher prediction yields for higher spectral intensities. The opposite was observed for DMY prediction with the hyperspectral band at 946 nm. As the 950 nm band is near the minor water absorption band at 970 nm, this band probably gains its importance as an indicator for canopy water content. As DMY is the difference of FMY and canopy water content, a combination of features representing canopy water content and FMY could support DMY prediction. The relationship of the hyperspectral band at 674 nm on DMY prediction was not

Figure 12. Accumulated Local Effects (ALE) plots of each hundred FMY (left) and DMY (right) sensor fusion models. Shown are the main effects (differences in prediction) of the four most important feature types (a type is the collection of e.g. all CSH features). ALE curves are calculated as median curve from each 100 model runs. Rug plots visualise the distribution of the feature values from each training data set, where each tick represents one of the 130 training samples (80 % of all samples) for all 100 model runs (13.000 ticks).

20563485, 2021, 2, Downloaded from https://zslpublications.onlinelibrary.wiley.com/doi/10.1002/rse2.182 by HEALTH RESEARCH BOARD, Wiley Online Library on [31/08/2024]. See the Terms and Conditions (https://onlinelibrary.wiley.com/terms-and-conditions) on Wiley Online Library for rules of use; OA articles are governed by the applicable Creative Commons License

Figure 13. Prediction map from random forest regression model of FMY (kg m^{-2}) of 8 × 8 m plots for each grassland type based on a random forest model using features from the hyperspectral and 3d laser dataset. White plots in *Trisetum flavescens* represent missing values.

explicitly positive nor negative (Fig. 12). We would expect high absorption rates of this wavelength by the photosynthetic light reactions of healthy vegetation. However, a high DMY can include biomass in non-healthy condition that has a lower absorption in this spectral range.

Point density is positively correlated with FMY and DMY. The high scanning resolution provides information from deep inside the canopy structure and, thereby, conducts detailed information about canopy density. A voxel feature with a voxel size of 0.245 m appears as an important feature in all models. This is in line with our previous research finding (Cooper et al., 2017; Wallace et al., 2017; Schulze-Brüninghoff et al., 2019). The good performance of voxel and point density features are due to the short distance between the terrestrial laser scanner position and the research plots as well as the combination of two point clouds generated from opposite scanner positions. This can compensate the occlusion effect and the bias by scanning distance. Mean elevation values correlate positively with biomass. This could be influenced by large lupine plants and other vegetation with increased canopy height, leading to a rough canopy surface which increases the elevation values. Canopy surface height was also found important and its positive correlation with biomass yields is well known (Zhang et al., 2018; Grüner et al., 2019).

To test if the presence of lupine leads to an under- or overprediction of FMY and DMY, the Normalized Deviations of predicted and measured FMY and DMY was used. It shows that lupine invaded sites are neither over- nor underpredicted. Lupine contributions between 20 % and 40 % have the lowest normalized deviation for both FMY and DMY prediction models. Lupines have a comparably complex vertical structure with overlapping leaves leading to occlusion of leaves and potential saturation of the biomass-reflectance relationship. As lupine plants usually have higher water contents than the surrounding grass vegetation (Hensgen and Wachendorf, 2016), it seems reasonable, that our machine learning model, based on spectral features, was able to incorporate this relationship.

The presence of many large lupine individuals on the usability of 3d laser features could be similar to the spectral features, considering a saturation point at a certain lupine contribution for certain laser features (e. g. point density, mean elevation). For example, point density could saturate, when the vegetation is so dense, that it prevents both of the opposite laser scans from detecting vegetation that is covered by large lupine plants.

When it comes to applied monitoring, TLS methods are rather ineffective. However, UAV-based LiDAR or mobile LiDAR systems may be a future-oriented avenue in this regard. Alternatively, 3d point cloud data, derived from UAV-based RGB images through structure from motion technique could be a reasonable way to collect simultaneously spectral and 3d information in one flight mission (Lussem et al., 2019). This could accelerate the data collection but with reduced point cloud density, compared to LiDAR systems (Wijesingha et al., 2019), especially below the top canopy, since photogrammetric point clouds are predominantly resembling the upper canopy layers only. The effect of lupine on model

accuracy needs further investigation. The potential of an additional classification step as described by (Wijesingha et al., 2020) before biomass prediction could be helpful to extrapolate the biomass prediction models in time and space.

Conclusion

The fusion of complementary sensor systems can increase the power to predict biomass yields of heterogenous and extensively managed grasslands. It is a novel alternative to labour-intensive, traditional biomass prediction methods and to remote sensing methods using only single sensor data. The chosen features from laser and hyperspectral data seemed a good combination to collect information of FMY and DMY.

Sites invaded by lupine had low normalized deviations compared to non-invaded. The lowest over- and under-prediction was found with lupine contributions between 20 and 40 %. The abundance of invasive species can impact the prediction quality of remote sensing based FMY and DMY prediction in extensively managed grasslands.

Acknowledgments

Conflict of Interest

The authors declare no conflict of interest.

References

Ali, I., F. Cawkwell, E. Dwyer, and S. Green. 2017. Modeling managed grassland biomass estimation by using multitemporal remote sensing data — a machine learning approach. *IEEE J. Select. Topics Appl. Earth Obs. Remote Sens.* 10, 3254–3264. https://doi.org/10.1109/JSTARS.2016.2561618

Apley, D.2018. ALEPlot: Accumulated Local Effects (ALE) Plots and Partial Dependence (PD) Plots. Available at https://cran.r-project.org/package=ALEPlot

Apley, D. W., and J. Zhu. 2019. 'Visualizing the effects of predictor variables in black box Su-', arXiv preprint, 1–44.

de Bello, F., S. Lavorel, S. Díaz, R. Harrington, J. H. C. Cornelissen, R. D. Bardgett, et al. 2010. Towards an assessment of multiple ecosystem processes and services via functional traits. *Biodivers. Conserv.* 19, 2873–2893. https://doi.org/10.1007/s10531-010-9850-9

Breiman, L. 1996. Out-of-bag estimation. Available at https://www.stat.berkeley.edu/~breiman/OOBestimation.pdf

Breiman, L. E. O. 2001. Random forests. *Mach. Learn.* 45, 5–32. https://doi.org/10.1023/A:1010933404324

Clevers, J. G. P. W., L. Kooistra, and M. E. Schaepman. 2008. International Journal of Applied Earth Observation and Geoinformation Using spectral information from the NIR water absorption features for the retrieval of canopy water content. *Int. J. Appl. Earth Obs. Geoinf.* 10(3), 388–397. https://doi.org/10.1016/j.jag.2008.03.003

Cooper, S. D., D. Roy, C. Schaaf, and I. Paynter. 2017. Examination of the potential of terrestrial laser scanning and structure-from-motion photogrammetry for rapid nondestructive field measurement of grass biomass. *Remote Sens.* 9(6), 531. https://doi.org/10.3390/rs9060531

Deutscher Wetterdienst. 2018. Available at: https://www.dwd.de/EN/Home/home_node.html (Accessed: 23 July 2018).

Evans, I. S. 1980. 'An integrated system of terrain analysis and slope mapping'. *Zeitschrift für Geomorphologie.* 36, 274–295.

Florinsky, I. V. 1998. Accuracy of local topographic variables derived from digital elevation models. *International Journal of Geographical Information Science* 12(1), 47–61. https://doi.org/10.1080/136588198242003

Genuer, R., J.-M. Poggi, and C. Tuleau-Malot. 2019. VSURF: Variable Selection Using Random Forests. Available at: https://cran.r-project.org/package=VSURF

Gewali, U. B., S. T. Monteiro, and E. Saber. 2018. Machine learning based hyperspectral image analysis: a survey. *ArXiv* preprint, 1–46. https://arxiv.org/abs/1802.08701

Grüner, E., T. Astor, and M. Wachendorf. 2019. Biomass prediction of heterogeneous temperate grasslands using an SfM approach based on UAV imaging. *Agronomy* 9(2), 54. https://doi.org/10.3390/agronomy9020054

Hackbart, J. 1961. Die Genzentren der Gattung Lupinus in der neuen Welt und ihre Bedeutung für die Züchtung. *Zeitschr. f. Pflanzenzüchtung* 46, 254–264.

Hensgen, F., and M. Wachendorf. 2016. The effect of the invasive plant species Lupinus polyphyllus Lindl. on energy recovery parameters of semi-natural grassland biomass. *Sustainability* 8(10), 998. https://doi.org/10.3390/su8100998

Hijmans, R. J.2019. raster: geographic geographic data analysis and modeling. R package version 2.8-19. Available athttps://cran.r-project.org/package=raster

Hiltbrunner, E., R. Aerts, T. Bühlmann, K. Huss-Danell, B. Magnusson, D. D. Myrold, et al. 2014. Ecological

consequences of the expansion of N 2 - fixing plants in cold biomes. *Oecologia* **176**, 11–24. https://doi.org/10.1007/s00442-014-2991-x

Karunaratne, S., A. Thomson, E. Morse-McNabb, J. Wijesingha, D. Stayches, A. Copland, et al. 2020. The fusion of spectral and structural datasets derived from an airborne multispectral sensor for estimation of pasture dry matter yield at paddock scale with time. *Remote Sens.* **12**(12), 2017. https://doi.org/10.3390/rs12122017

Kindinger, W. 1942. 'Beiträge zur Entwicklung der Kulturlandschaft der zentralen Rhön vom dreißigjährigen Krieg bis 1933', *Fränkische Studien 4*.

Kong, B., H. Yu, R. Du, and Q. Wang. 2019. Rangeland ecology & management quantitative estimation of biomass of alpine grasslands using hyperspectral remote sensing. *Rangel. Ecol. Manag.* **72**(2), 336–346. https://doi.org/10.1016/j.rama.2018.10.005

Kuhn, M. 2008. Building predictive models in R using the caret Package. *J. Stat. Softw.* **28**(5), 1–26. http://dx.doi.org/10.18637/jss.v028.i05

Lecigne, B., S. Delagrange, and C. Messier. 2014. VoxR: metrics extraction of trees from T-LiDAR data. Available at https://cran.r-project.org/package=VoxR

Lussem, U., A. Bolten, J. Menne, M. L. Gnyp, J. Schellberg, and G. Bareth. 2019. Estimating biomass in temperate grassland with high resolution canopy surface models from UAV-based RGB images and vegetation indices. *J. Appl. Remote Sens.* **13**(03), 1. https://doi.org/10.1117/1.JRS.13.034525

Moeckel, T., H. Safari, B. Reddersen, T. Fricke, and M. Wachendorf. 2017. Fusion of ultrasonic and spectral sensor data for improving the estimation of biomass in grasslands with heterogeneous sward structure. *Remote Sens.* **9**(1), 98. https://doi.org/10.3390/rs9010098

Otte, A., and P. Maul. 2005. Verbreitungsschwerpunkte und strukturelle Einnischung der Stauden-Lupine (*Lupinus polyphyllus* Lindl.) in Bergwiesen der Rhön. *Tuexenia* **25**, 151–182.

R Core Team. 2019. *R: A language and environment for statistical computing*. R Foundation for Statistical Computing, Vienna. Available at: https://www.r-project.org/

Rouse, J. W., R. H. Haas, J. A. Schell, and D. W. Deering. 1974. 'Monitoring Vegetation Systems in the Great Plains with ERTS', Proceedings Third ERTS Symposium, NASA SP-351, 10–14 December 1973, Washington, DC (Washington: NASA Scientific and Technical Information Office), pp. 309–317.

Schulze-Brüninghoff, D., F. Hensgen, M. Wachendorf, and T. Astor. 2019. Methods for LiDAR-based estimation of extensive grassland biomass. *Comput. Electron. Agr.* **156**, 693–699. https://doi.org/10.1016/j.compag.2018.11.041

Silleos, G., T. K. Alexandridis, I. Z. Gitas, K. Perakis. 2006. Vegetation indices: advances made in biomass estimation and vegetation monitoring in the last 30 years. *Geocarto Int.* **21**, 21–28.

Smit, H. J., M. J. Metzger, and F. Ewert. 2008. Spatial distribution of grassland productivity and land use in Europe. *Agr. Syst.* **98**(3), 208–219. https://doi.org/10.1016/j.agsy.2008.07.004

Sun, L., Z. Wu, J. Liu, L. Xiao, and Z. Wei. 2015. 'Supervised spectral-spatial hyperspectral image classification with weighted markov random fields'. *IEEE Trans. Geosci. Remote Sens.* **53**(3), 1490–1503. https://doi.org/10.1109/TGRS.2014.2344442

Swatantran, A., R. Dubayah, D. Roberts, M. Hofton, and J. B. Blair. 2011. Remote Sensing of Environment Mapping biomass and stress in the Sierra Nevada using lidar and hyperspectral data fusion. *Remote Sens. Environ.* **115**(11), 2917–2930. https://doi.org/10.1016/j.rse.2010.08.027

Valtonen, A., J. Jantunen, and K. Saarinen. 2006. Flora and lepidoptera fauna adversely affected by invasive *Lupinus polyphyllus* along road verges. *Biol. Cons.* **133**(3), 389–396. https://doi.org/10.1016/j.biocon.2006.06.015

Vilà, M., J. L. Espinar, M. Hejda, P. E. Hulme, V. Jarošík, J. L. Maron, et al. 2011. Ecological impacts of invasive alien plants: a meta-analysis of their effects on species, communities and ecosystems. *Ecol. Lett.* **14**, 702–708. https://doi.org/10.1111/j.1461-0248.2011.01628.x

Volz, H. 2003. Ursachen und Auswirkungen der Ausbreitung von Lupinus polyphyllus Lindl. im Bergwiesenökosystem der Rhön und Maßnahmen zu seiner Regulierung. Justus-Liebig-Universität Gießen. Available at: urn:nbn:de:gbv:27-20061101-100747-8.

Wachendorf, M., T. Fricke, and T. Möckel. 2017. Remote sensing as a tool to assess botanical composition, structure, quantity and quality of temperate grasslands. *Grass Forage Sci.* **73**, 1–14. https://doi.org/10.1111/gfs.12312

Wallace, L., S. Hillman, K. Reinke, and B. Hally. 2017. Non-destructive estimation of above-ground surface and near-surface biomass using 3D terrestrial remote sensing techniques. *Methods Ecol. Evol.* **8**(11), 1607–1616. https://doi.org/10.1111/2041-210X.12759

Wang, C., S. Nie, X. Xi, S. Luo, and X. Sun. 2017. Estimating the biomass of maize with hyperspectral and LiDAR data. *Remote Sens.* **9**(1), 1–12. https://doi.org/10.3390/rs9010011

Weiss, M., F. Jacob, and G. Duveiller. 2020. Remote Sensing of Environment Remote sensing for agricultural applications: a meta-review. *Remote Sens. Environ.*. **236**, 111402. https://doi.org/10.1016/j.rse.2019.111402

White, J. C., N. C. Coops, M. A. Wulder, M. Vastaranta, T. Hilker, P. Tompalski. 2016. Remote sensing technologies for enhancing forest inventories: a review remote sensing technologies for enhancing forest inventories: a review. *Can. J. Remote. Sens.* **42**(5), 619–641. https://doi.org/10.1080/07038992.2016.1207484

Wijesingha, J., T. Astor, D. Schulze-Brüninghoff, and M. Wachendorf. 2020. Mapping invasive *Lupinus polyphyllus* Lindl. in semi-natural grasslands using object-based image analysis of UAV-borne images. *PFG – J. Photogram. Remote*

Sens. Geoinform. Sci. https://doi.org/10.1007/s41064-020-00121-0

Wijesingha, J., T. Moeckel, F. Hensgen, and M. Wachendorf. 2019. 'Evaluation of 3D point cloud-based models for the prediction of grassland biomass'. *Int J Appl Earth Observ Geoinform* **78**, 352–359. https://doi.org/10.1016/J.JAG.2018.10.006

Xue, J., and B. Su. 2017. Significant remote sensing vegetation indices: a review of developments and applications', 2017, pp. 1–17. https://doi.org/10.1155/2017/1353691

Yue, J., G. Yang, C. Li, Z. Li, Y. Wang, H. Feng, et al. 2017. Estimation of winter wheat above-ground biomass using unmanned aerial vehicle-based snapshot hyperspectral sensor and crop height improved models. *Remote Sens.* **9**(7), 708. https://doi.org/10.3390/rs9070708

Zhang, H., Y. Sun, L. Chang, Y. Qin, J. Chen, Y. Qin, et al. 2018. Estimation of grassland canopy height and aboveground biomass at the quadrat scale using unmanned aerial vehicle. *Remote Sens.* **10**(6), 851. https://doi.org/10.3390/rs10060851

Supporting Information

Additional supporting information may be found online in the Supporting Information section at the end of the article.

Tables S1. Summary of all features derived from terrestrial laser scanner and hyperspectral camera, before and after feature selection.

Tables S2. Summary statistics of reference FMY and DMY data.

Tables S3. Information on fresh matter (FMY) and dry matter (DMY) yield and lupine contribution for each grassland type and harvesting date.

Figure S1. Plot of fit of model build from sensor fusion data for FMY (left) and DMY (right). Each plot shows RFR

Figure S2. Normalised spectral reflectance curves of all samples coloured by FMY and DMY (kg m^{-2}).